

# Magnetic field and ISM in the local Galactic disc

Y. Sofue<sup>1</sup>\* H. Nakanishi<sup>2</sup>, and K. Ichiki<sup>3</sup>,

1. Institute of Astronomy, The University of Tokyo, Tokyo 181-0015, Japan

2. Graduate Schools of Sci. and Engineering, Kagoshima Univ., Kagoshima 890-8544, Japan

3. Graduate School of Science, Div. Particle and Astrophys. Sci., Nagoya University, Nagoya 464-8602, Japan

## ABSTRACT

Correlation analysis is obtained among Faraday rotation measure, HI column density, thermal and synchrotron radio brightness using archival all-sky maps of the Galaxy. A method is presented to calculate the magnetic strength and its line-of-sight (LOS) component, volume gas densities, effective LOS depth, effective scale height of the disk from these data in a hybrid way. Applying the method to archival data, all-sky maps of the local magnetic field strength and its parallel component are obtained, which reveal details of local field orientation.

**Key words:** galaxies: individual (Milky Way) — ISM: general — ISM: magnetic field

## 1 INTRODUCTION

Large scale mappings of Faraday rotation measure (RM) of extragalactic linearly polarized radio sources have been achieved extensively in the decades (Taylor et al 2009; Oppermann et al. 2012), with which various analyses have been obtained to investigate structures of galactic as well as intergalactic magnetic fields (e.g., review by Akahori et al. 2018).

Local magnetic fields in the Solar vicinity have been also studied using these RM data as well as polarization observations of the Galactic radio emission (Mao et al. 2012; Wolleben et al. 2010; Stil et al. 2011; Sun et al. 2015; Sofue and Nakanishi 2017; Liu et al. 2017; Van Eck et al. 2017 Alves et al. 2018).

Synchrotron radio emission is a tool to measure the total strength of magnetic field on the assumption that the magnetic energy-density (pressure) is in equipartition with the thermal and cosmic ray energy densities (e.g., Sofue et al. 1986). This method requires information about the depth of emitting region in order to calculate the synchrotron emissivity per volume, as the intensity is an integration of the emissivity along the line of sight (LOS).

Rotation measure is an integration of the parallel component of magnetic field multiplied by thermal electron density along the line-of-sight (LOS). It is related not only to thermal (free-free) radio emission, but also to HI column density through thermal electron fraction in the neutral interstellar medium (ISM).

Determination of the LOS depth is, therefore, a key to measure the magnetic strength from synchrotron emission and the parallel magnetic component from RM. The depth is also required to estimate the volume densities of HI and thermal electrons from observed HI and thermal radio intensities. Emission measure and HI column density are useful to estimate the LOS depth, given a relation between the thermal and HI gas densities is appropriately settled.

In this paper, correlation analyses are obtained among various radio astronomical observables (RM, HI column density, thermal and synchrotron radio brightness) in order to determine physical quantities of the ISM such as the magnetic strength, gas densities, and LOS depth. One of the major goal of the present hybrid analysis method will be to obtain whole-sky maps of the total strength and parallel component of the magnetic field in the local Galactic disk.

## 2 OBSERVABLES AND CORRELATIONS

### 2.1 Data

The observational data for the Faraday rotation were taken from all-sky RM survey by Taylor et al. (2009), HI data from the Leiden-Argentine-Bonn (LAB) survey by Kalberla et al. (2005), synchrotron and free-free emissions at 23 GHz from the 7-years result of Wilkinson Microwave Anisotropy Probe (WMAP) project by Gold et al (2011). Figure 1 shows the employed map data for  $RM$ ,  $|RM|$ , HI column density  $N_{\text{HI}}$ , thermal (free-free) radio brightness temperature  $T_{\text{ff}}$  and synchrotron radio brightness  $T_{\text{syn}}$ , both at 23 GHz.

Figure 2 shows plots of the same data in figure 1 against the latitude  $b$  and cosec  $|b|$ . The global similarity of the latitudinal variations indicates that the four observed quantities are deeply coupled with each other. It is remarkable that all the plots beautifully obey the cosec  $|b|$  relation shown by the full lines. This fact indicates that these radio observed quantities are tightly coupled with the line-of-sight depth (LOS) through galactic disk composed of a plane parallel layer in the first approximation.

A more detailed inspection of the figures reveals that, besides the global common cosec  $|b|$  property, there exist systematic differences in the latitudinal variations among the quantities. The rotation measure,  $RM$ , shows milder increase toward the galactic plane than the other quantities. The saturation of  $|RM|$  near the galactic plane suggests that the magnetic field directions are reversing there. On

\*E-mail:sofue@ioa.s.u-tokyo.ac.jp

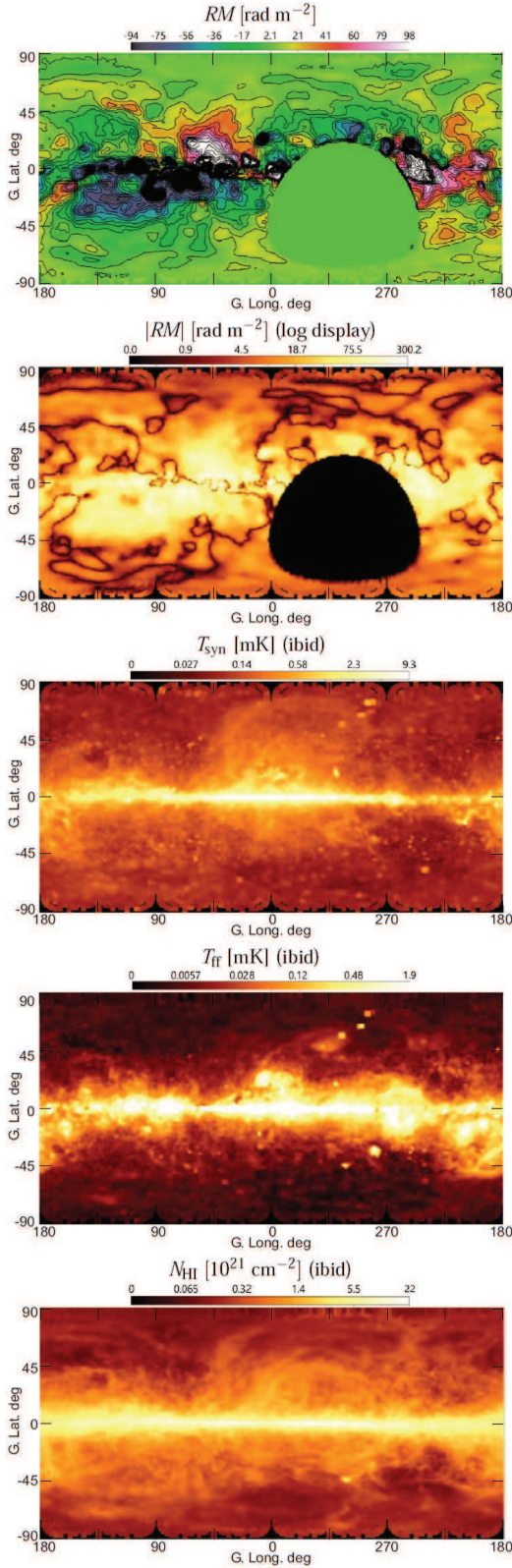


**Figure 1.** All-sky maps of  $RM$ ,  $|RM|$  ( $\text{rad m}^{-2}$ ) (Taylor et al. 2009),  $T_{\text{syn}}$  and  $T_{\text{HI}}$  (mK) at 23 GHz (Gold et al 2011), and  $N_{\text{HI}}$  ( $10^{21} \text{ cm}^{-2}$ ) (Kalberla et al. 2005).

the other hand, synchrotron intensity has much sharper peak at the plane, and shows similar variation to HI intensity. Another remarkable property is the sharper increase of the thermal emission toward the galactic plane than HI. This manifests stronger dependence of the thermal emission on the ISM density through the emission measure  $EM \propto n_e^2 L$  than that of the HI column  $N_{\text{HI}} \propto n_{\text{HI}} L$ .

The radio observables are related to the ISM quantities as follows. Faraday rotation measure  $RM$  is related to the thermal electron density  $n_e$  and line-of-sight (LOS) component of the magnetic field strength  $B_{\parallel}$  through

$$\left( \frac{RM}{\text{rad m}^{-2}} \right) \sim 0.81 \left( \frac{\langle n_e \rangle}{\text{cm}^{-3}} \right) \left( \frac{\langle B_{\parallel} \rangle}{\mu\text{G}} \right) \left( \frac{L}{\text{pc}} \right). \quad (1)$$

The emission measure  $EM$  is rewritten by the volume density  $n_e$  of thermal electrons as

$$\left( \frac{EM}{\text{pc cm}^{-6}} \right) \sim \left( \frac{\langle n_e \rangle}{\text{cm}^{-3}} \right)^2 \left( \frac{L}{\text{pc}} \right). \quad (2)$$

The HI column density  $N_{\text{HI}}$  is given by the HI volume density  $n_{\text{HI}}$  as

$$\left( \frac{N_{\text{HI}}}{\text{cm}^{-2}} \right) \sim 3.086 \times 10^{18} \left( \frac{\langle n_{\text{HI}} \rangle}{\text{cm}^{-3}} \right) \left( \frac{L}{\text{pc}} \right). \quad (3)$$

Here,  $\langle \rangle$  denotes LOS average, and is defined and described later. The synchrotron radio brightness  $\Sigma_{\nu}$ , as observed by the brightness temperature  $T_{\text{syn}}$ , is related to the volume emissivity  $\epsilon$ , frequency  $\nu$ , and  $L$  as

$$\Sigma_{\nu} = \frac{2kT_{\text{syn}}}{\lambda^2} \sim \frac{L}{4\pi} \frac{d\epsilon}{d\nu} \sim \frac{L}{4\pi} \frac{\epsilon}{\nu}, \quad (4)$$

which may be rewritten in a practical way as

$$\left( \frac{T_{\text{syn}}}{\text{K}} \right) \sim 1.472 \times 10^{11} \left( \frac{\nu}{\text{GHz}} \right)^{-3} \left( \frac{\epsilon}{\text{erg cm}^{-3} \text{s}^{-1}} \right) \left( \frac{L}{\text{pc}} \right), \quad (5)$$

where  $\lambda = c/\nu$  is the wavelength and  $k$  is the Boltzmann constant.

We assume that the Galactic disk is composed of four horizontal layers (disks) of HI gas, thermal electrons, magnetic fields and cosmic rays, which have the same half thickness (scale height)  $z_{1/2:\text{disk}}$ . This means that the LOS depth  $L$  of the four quantities are equal. This assumption may not be good enough for the synchrotron emission that may originate from a thicker magnetic halo. However, it may be considered that the contribution of magnetic halo to  $RM$  and synchrotron emission is much smaller than that of the disk because of weaker magnetic strength and electron density by an order of magnitude. The here used depth  $L$  is an effective depth, and is related to the geometrical depth through a volume filling factor, as will be described later in detail.

Based on these considerations, we assume that the ISM quantities are smooth functions of the effective LOS depth  $L$  for the first approximation, and an average of any quantity  $f$  over  $L$  satisfies the following relation,

$$\langle f \rangle = \frac{\int_0^L f dx}{\int_0^L dx} = \frac{\int_0^L f dx}{L}. \quad (6)$$

We also assume for any quantities  $f$  and  $g$

$$\langle f \rangle \sim \langle f^2 \rangle^{1/2}, \quad (7)$$

and

$$\langle fg \rangle \sim \langle f \rangle \langle g \rangle. \quad (8)$$

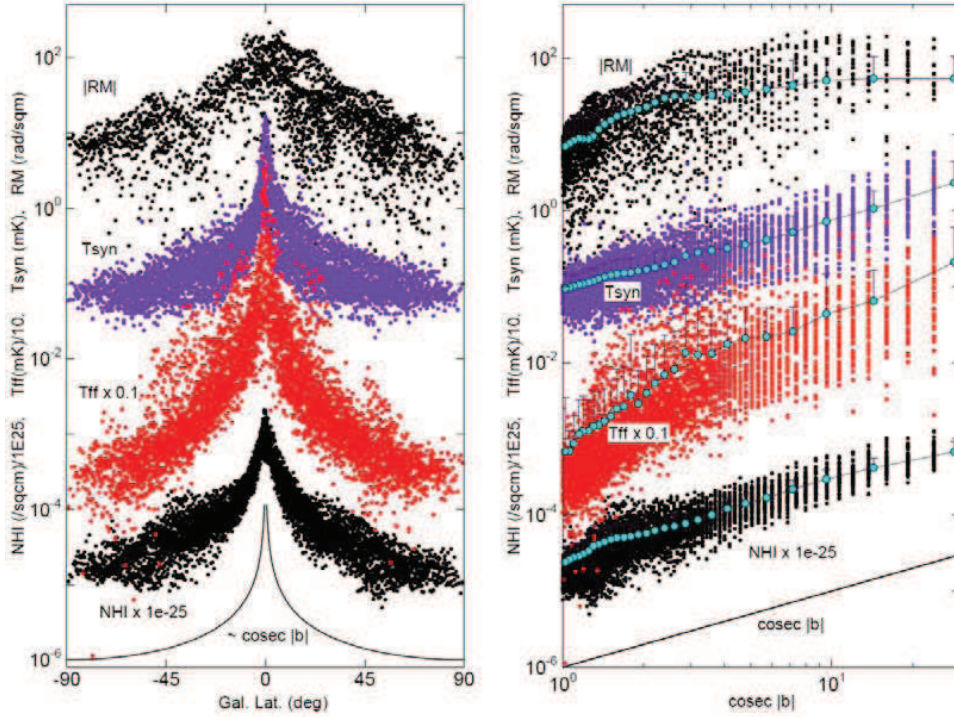


**Figure 2.**  $|RM|$  (rad  $m^{-2}$ ),  $T_{\text{syn}}$  (mK),  $0.1 \times T_{\text{ff}}$  (mK) and  $10^{-25} \times N_{\text{HI}}$  ( $\text{cm}^{-2}$ ) plotted against latitude  $b$ . Points are reduced by 1 per 10. Note the beautiful dependence of the plotted quantities on  $\text{cosec } |b|$  relation shown by the full lines, indicating that they are tightly coupled with the line-of-sight depth of a plane parallel layer. Right panel shows the same, but against  $\text{cosec } |b|$ . Open circles are averages of the plots in every  $2^\circ$  bin of absolute latitude. Bars show standard deviations (sd) of the original values, which are given only in upper sides in order to avoid logarithm of negative values for large sd.

## 2.2 Correlation among Radio Observables

### 2.2.1 Free-Free to HI tight relation

Figure 3(a) shows a plot of  $T_{\text{ff}}$  against the square of  $N_{\text{HI}}$ . The straight line indicates a  $T_{\text{ff}} \propto N_{\text{HI}}^2$ , and plots on the log-log space well obeys this proportionality. This relation indicates that the thermal electron density  $\langle n_e \rangle$  is approximately proportional to  $\langle n_{\text{HI}} \rangle$ , if  $L$  is not strongly variable from point to point, which is indeed the case except for the high  $N_{\text{HI}}$  region close to the galactic plane. This correlation will be used to estimate the electron density from HI column.

### 2.2.2 Synchrotron to ISM relation

Figure 3(b) is a plot of  $T_{\text{syn}}$  against  $N_{\text{HI}}$ . High intensity region is approximately represented by a power law of index  $7/4$ ,  $T_{\text{syn}} \propto N_{\text{HI}}^{7/4}$ , as expected from frozen-in magnetic field into the ISM and energy-density equipartition between the magnetic field, cosmic rays, and ISM (see Appendix). Plot of  $T_{\text{syn}}$  against  $T_{\text{ff}}$  in (c) shows a similar relation, where  $T_{\text{syn}} \propto T_{\text{ff}}^{7/8}$  is expected from the equipartition, because  $N_{\text{HI}} \propto T_{\text{ff}}^{1/2}$ . In both plots, the synchrotron emission tends to exceed the energy equipartition lines at low intensity regions (high latitudes). This yields larger uncertainty of the estimated magnetic strength at high latitudes.

### 2.2.3 RM to ISM relation

Figure 4 shows plots of the absolute RM values against (a)  $N_{\text{HI}}$ , (b)  $T_{\text{syn}}$  and (c)  $T_{\text{ff}}$ . It is impressive that the plots are more scattered than those in figure 3. This is because the rotation measure is an integrated function of the magnetic field strength along the LOS including the reversal of field direction. This scattered characteristics of RM is useful to derive the spatial variation of the LOS field direction and strength  $B_{\parallel}$ .

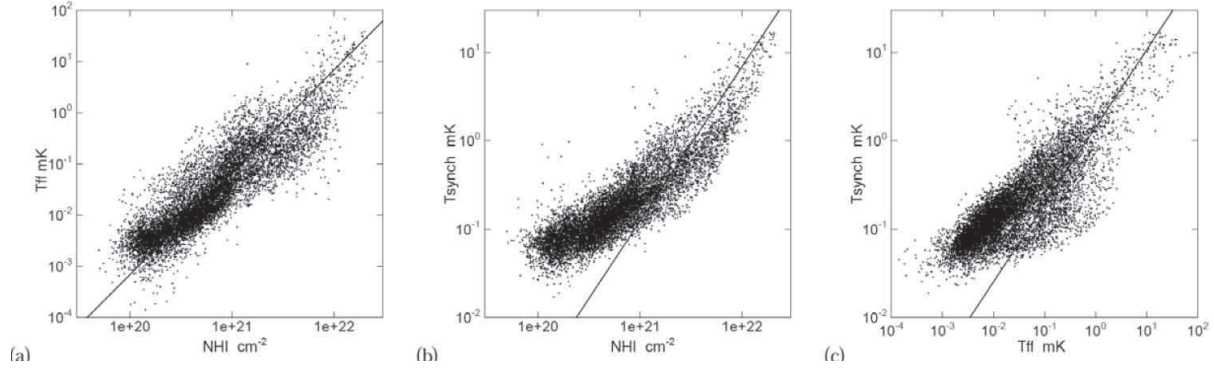
Although  $|RM|$  is scattered against the other ISM observables in the whole-sky data, it may better be correlated in a narrower restricted region. Figure 5 shows an example of plots of  $|RM|$ ,  $T_{\text{syn}}$  and  $T_{\text{ff}}$  against  $N_{\text{HI}}$  in a small area in the 1st quadrant of the Galaxy at  $30^\circ \leq l \leq 50^\circ$  and  $b \geq 0^\circ$ . Shown by green circles are latitudes corresponding to individual  $N_{\text{HI}}$  data points, indicating the tight dependence of  $N_{\text{HI}}$  on the latitude through LOS depths. This figure demonstrates how  $|RM|$  is tightly correlated to  $N_{\text{HI}}$  in a restricted area.

Figure 6 shows plots of  $RM$  against galactic latitude and HI column in the 1st quadrant of the Galaxy. Grey dots show all points, and blue and red dots represent those in northern and southern two small regions in the same quadrant at  $30^\circ \leq l \leq 60^\circ$  and  $b \geq 10^\circ$  and at  $30^\circ \leq l \leq 60^\circ$  and  $b \leq -10^\circ$ .

Absolute RM value increases toward the galactic plane, the sign of RM changes from negative to positive as the latitude increases, which indicates sudden reversal of the magnetic field direction. The bottom panel in the figure represents the same phenomenon in terms of the column density of HI gas.

Linear relation of RM with HI column is found in low  $|RM|$  and  $N_{\text{HI}}$  regions. However, the linearity is lost toward the galactic





**Figure 3.** Correlation of  $T_{\text{ff}}$  and  $N_{\text{HI}}$  with a line of power index 2,  $T_{\text{syn}}$  and  $N_{\text{HI}}$  with a line of index 8/7. Vertical scaling of the lines are arbitrary.

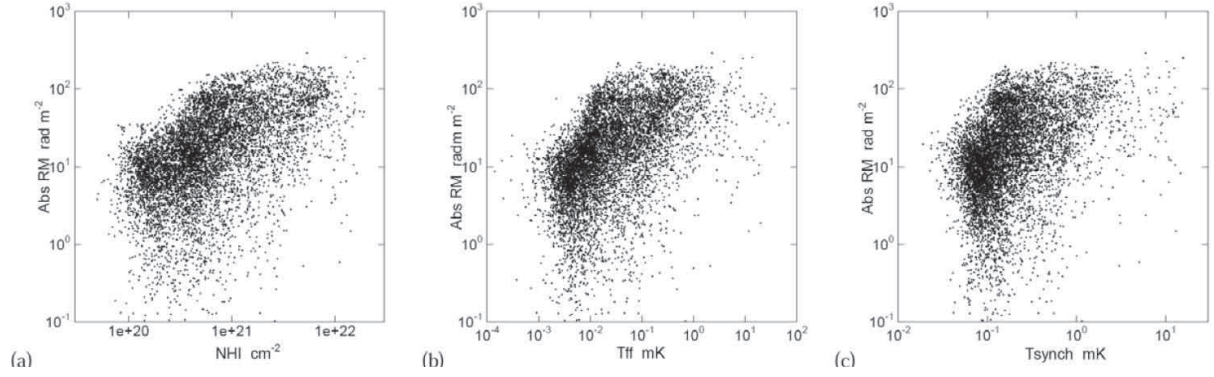


**Figure 4.** Correlation of  $|RM|$  with (a) HI, (b) FF and (c) Synchrotron emissions.

plane at  $|b| \lesssim 10^\circ$  with increasing  $N_{\text{HI}}$ . This represents decrease in the LOS component of magnetic strength  $|B_{\parallel}|$  toward the plane, which indicates rapid change of the field direction near the plane.

### 3 GAS DENSITIES, LINE-OF-SIGHT DEPTH, AND DISK THICKNESS

Given the four radio observables ( $RM$ ,  $T_{\text{ff}}$ ,  $T_{\text{syn}}$ , and  $N_{\text{HI}}$ ), four ISM parameters (averaged electron density  $\langle n_e \rangle \sim x_e n_{\text{HI}}$ , effective LOS depth  $L$ , total magnetic intensity  $B$ , and LOS component of magnetic field  $B_{\parallel}$ ) can be estimated as follows. Figure 7 illustrates the flow of the analysis, which we call the ISM hybrid. The effective depth  $L$  will be related to geometrical scale height of the disk through volume filling factor.

#### 3.1 Thermal electron density

Thermal electron density is assumed to be proportional to the HI gas density as

$$n_e = x_e n_{\text{HI}}, \quad (9)$$

where,  $x_e$  is the thermal electron fraction in the neutral ISM,

$$x_e = \frac{\langle n_e \rangle}{\langle n_e \rangle + \langle n_{\text{HI}} \rangle} \sim \frac{\langle n_e \rangle}{\langle n_{\text{HI}} \rangle}, \quad (10)$$

which is assumed to be  $x_e \sim 0.1$  after Foster et al. (2013), who obtained  $x_e \sim 0.08$ . Local HI gas is considered to be in cold phase from recent measurement of spin temperature (Sofue 2017, 2018).

Even if warm HI is contaminated, its density is an order of magnitude lower, so that the column density is not much affected by warm HI, unless the scale height of warm HI is an order of magnitude greater than that of cold HI.

Electron density is obtained by dividing the emission measure by column density of electrons, which is related to HI column, or  $n_e \sim (n_e^2 L) / (n_e L) \sim (n_e^2 L) / (x_e n_{\text{HI}} L) \sim EM / (x_e N_{\text{HI}})$ . Thus, we have

$$\begin{aligned} \left( \frac{\langle n_e \rangle}{\text{cm}^{-3}} \right) &\sim 3.09 \times 10^{-3} \left( \frac{EM}{\text{pc cm}^{-6}} \right) \left( \frac{x_e N_{\text{HI}}}{10^{21} \text{ cm}^{-2}} \right)^{-1} \\ &\sim 6.82 \times 10^2 x_e^{-1} \left( \frac{N_{\text{HI}}}{10^{21} \text{ cm}^{-2}} \right)^{-1} \left( \frac{T_{\text{ff}}}{\text{K}} \right)_{23\text{GHz}} \end{aligned} \quad (11)$$

at  $\nu = 23$  GHz, where the following relations were used. The emission measure is expressed by  $T_{\text{ff}}$ , electron temperature ( $T_e \sim 10^4$  K), and observing frequency ( $\nu = 23$  GHz) as

$$\begin{aligned} \left( \frac{EM}{\text{pc cm}^{-6}} \right) &= 3.05 \times 10^2 \left( \frac{T_{\text{ff}}}{\text{K}} \right) \left( \frac{T_e}{10^4 \text{ K}} \right)^{0.35} \left( \frac{\nu}{\text{GHz}} \right)^{2.1} \\ &\sim 2.21 \times 10^5 \left( \frac{T_{\text{ff}}}{\text{K}} \right)_{23\text{GHz}}, \end{aligned} \quad (12)$$

for  $T_e = 10^4$  K and  $\nu = 23$  GHz, where optical depth is given by (Oster 1961),

$$\tau = 3.28 \times 10^{-7} \left( \frac{T_e}{10^4 \text{ K}} \right)^{-1.35} \left( \frac{\nu}{\text{GHz}} \right)^{-2.1} \left( \frac{EM}{\text{pc cm}^{-6}} \right), \quad (13)$$

which is related to  $T_{\text{ff}}$  for optically thin case as

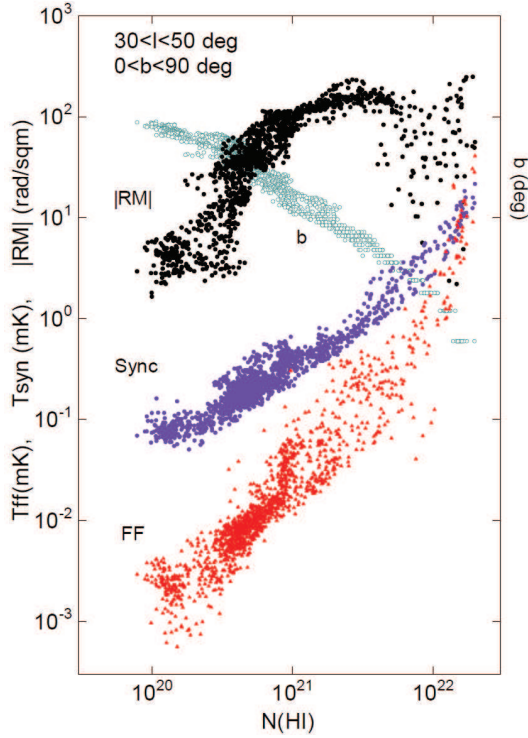


**Figure 5.** Correlations of  $|RM|$ ,  $T_{\text{ff}}$  and  $T_{\text{syn}}$  with  $N_{\text{HI}}$  in a restricted area on the sky ( $30^\circ \leq l \leq 50^\circ$ ,  $b \geq 0^\circ$ ). Shown by green circles are latitudes with the values indicated by the right axis

$$T_{\text{ff}} = (1 - e^{-\tau})T_e \simeq \tau T_e. \quad (14)$$

Figure 8 shows a calculated all-sky map of  $n_{\text{HI}}$ , which is equal to  $n_e/x_e$ , using equation (12). The derived HI density at  $|b| > \sim 10^\circ$  has nearly a constant value around  $\sim 1 - 2 \text{ cm}^{-3}$ , except for clumpy regions and the GC.

### 3.2 LOS depth, scale height, and volume filling factor

Recalling that  $N_{\text{HI}} \sim Ln_{\text{HI}}$  and  $EM \sim Ln_e^2 \sim Lx_e^2 n_{\text{HI}}^2$ , the LOS depth  $L$  is given by

$$\begin{aligned} \left(\frac{L}{\text{pc}}\right) &\sim 1.05 \times 10^5 \left(\frac{x_e N_{\text{HI}}}{10^{21} \text{ cm}^{-2}}\right)^2 \left(\frac{EM}{\text{pc cm}^{-6}}\right)^{-1} \\ &\sim 0.475 \left(\frac{x_e N_{\text{HI}}}{10^{21} \text{ cm}^{-2}}\right)^2 \left(\frac{T_{\text{ff}}}{\text{K}}\right)_{23\text{GHz}}^{-1}. \end{aligned} \quad (15)$$

Figure 9 shows the derived  $L$  plotted against  $N_{\text{HI}}$  for  $x_e = 0.1$ . The plot roughly obeys the linear relation,  $N_{\text{HI}} \propto L$ , indicated by the straight line, while points are largely scattered.

The here defined  $L$  is an "effective (physical)" LOS depth, and is related to the effective half thickness (scale height) of the disk,  $z_{1/2}$ , by

$$L = z_{1/2} \text{cosec } |b|. \quad (16)$$

The effective half thickness is further related to the 'geometrical' half thickness

$$z_{1/2} = \eta^{1/3} z_{1/2;\text{disk}}, \quad (17)$$

where  $\eta$  is the volume filling factor of the ISM. The factor  $\eta$  will

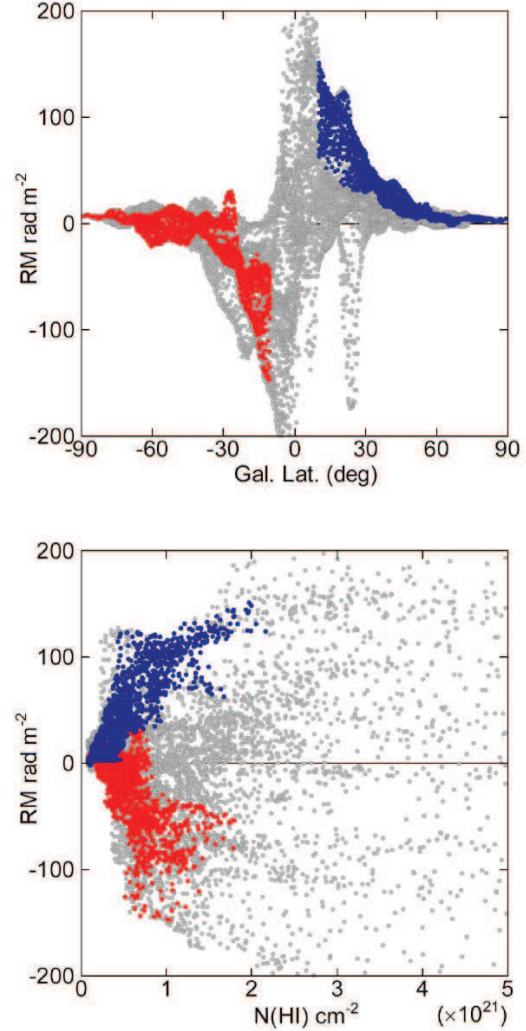


**Figure 6.** RM against galactic latitude (top) and HI column density (bottom) in the 1st quadrant of the Galaxy. Grey circles show all data points, blue dots are for a small region at  $30^\circ \leq l \leq 60^\circ$  and  $b \geq 10^\circ$  and red for  $30^\circ \leq l \leq 60^\circ$  and  $b \leq -10^\circ$  in the same quadrant.

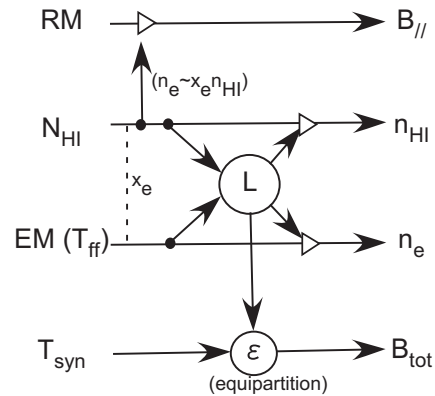


**Figure 7.** ISM hybrid for determination of physical quantities in the local disk from multiple radio observables.

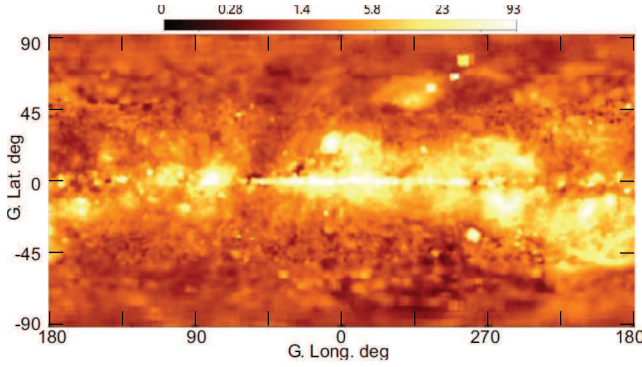


**Figure 8.** Logarithmic display of the volume density map of HI and thermal electrons. Shown is  $\langle n_{\text{HI}} \rangle$  [ $\text{cm}^{-3}$ ], which is assumed to be proportional to thermal electron density as  $\langle n_e \rangle \sim x_e \langle n_{\text{HI}} \rangle$  [ $\text{cm}^{-3}$ ] with  $x_e \sim 0.1$ .

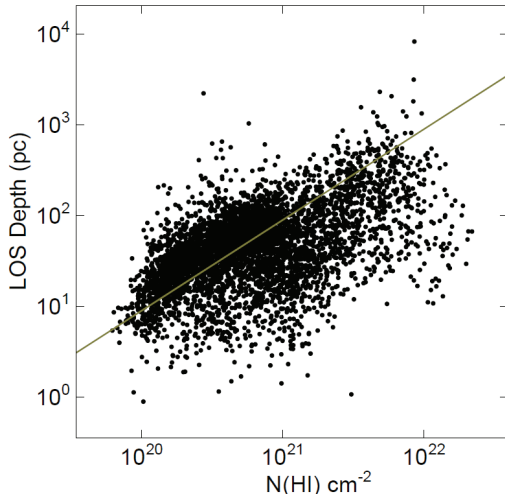


**Figure 9.** Effective LOS depth  $L$  of HI gas for  $x_e = 0.1$  plotted against  $N_{\text{HI}}$ . The straight line indicates a linear relation,  $N_{\text{HI}} \propto L$ , with arbitrary vertical scaling.

be determined using these relations referring to independent measurement of the HI disk scale height.

Figure 10 shows calculated  $z_{1/2}$  against latitude. Original data points are shown by gray dots, and averaged values in latitudinal interval of  $\Delta b = \pm 5^\circ$  are shown by big dots with standard errors. Points without error bar indicate those, whose errors are greater than the averaged values. The averaged effective half thickness tends to a constant of  $z_{1/2} \sim 60 \pm 8$  pc at  $40^\circ \leq |b| \leq 80^\circ$ .

From the current measurements of HI disk half thickness (160 pc, Lockman (1984); 150 pc, Wouterloot et al. (1990); 200 pc, Levine et al. (2006); 173 pc, Kalberla et al. (2007); 200 pc, Nakanishi and Sofue (2016); 217 pc, Marasco et al. (2017)), we adopt a simple average of the authors' values,  $z_{1/2;\text{disk}} = 183 \pm 26$  pc. In order for the present determination of  $z_{1/2}$  to satisfy equation (17), we obtain  $\eta \sim (z_{1/2}/z_{1/2;\text{disk}})^3 = 0.035 \pm 0.007$ . This value agrees with the recent determination for cold HI gas by Fukui et al. (2018).

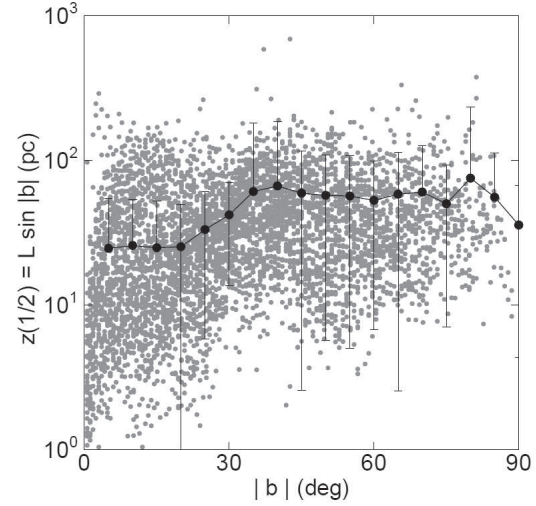


**Figure 10.** "Effective" half thickness (scale height) of the HI disk defined by  $z_{1/2} = L \sin |b|$  plotted against latitude, which is related to geometrical half thickness  $z_{1/2;\text{disk}}$  by  $z_{1/2} \sim \eta^{1/3} z_{1/2;\text{disk}}$  with  $\eta$  being the volume filling factor of the gas. Circles are averages of the neighboring latitude points with standard errors by bars. Points without bar indicate errors greater than the averaged values.

## 4 MAGNETIC FIELDS

### 4.1 Parallel component

The LOS (or parallel) component of the magnetic field can be obtained by dividing RM by the column density of thermal electrons as

$$\left\langle \frac{B_{\parallel}}{\mu\text{G}} \right\rangle \sim 3.81 \times 10^{-3} \left( \frac{RM}{\text{rad m}^{-2}} \right) \left( \frac{x_e N_{\text{HI}}}{10^{21} \text{ cm}^{-2}} \right)^{-1}. \quad (18)$$

It is stressed that this formula yields  $\langle B_{\parallel} \rangle$  directly from the observables  $RM$  and  $N_{\text{HI}}$  without employing the LOS depth  $L$ . So,  $\langle B_{\parallel} \rangle$  is the most accurate quantity determined in this paper.

Equation (18) is particularly simple and useful to estimate the parallel component of magnetic strength, because it includes only two observables,  $RM$  and  $N_{\text{HI}}$ , where the effective LOS depth  $L$  has been canceled out, leaving  $x_e$  as one parameter to be assumed. This relation is now applied for mapping of the  $B_{\parallel}$  value on the sky assuming  $x_e = 0.1$ .

First, the sky is binned into  $1^\circ$  degree grids in longitude and latitude, and calculate averages of  $RM$  and  $N_{\text{HI}}$  values within  $\pm 1^\circ$  about each grid point for  $|b| \leq 50^\circ$  region, and within  $\pm 2^\circ$  for  $|b| > 50^\circ$ . At each point on the grids,  $\langle B_{\parallel} \rangle$  is calculated with the aid of equation (18). By this procedure a  $361 \times 181$  meshed map of  $\langle B_{\parallel} \rangle$  is obtained on the sky with a resolution of  $1 - 2^\circ$ .

Figure 11 shows the thus obtained all-sky map of  $\langle B_{\parallel} \rangle$ . Positive value in red color indicates a magnetic field away from the observer, and negative with blue indicates a field approaching the observer.

Let us remember that the RM map was strongly affected by the peaked line-of-sight depth near the galactic plane, causing large positive and negative values near the plane. This caused steep latitudinal gradient of RM due to the field reversal from north to south, resulting in RM singularity along the galactic plane.

On the other hand, the  $\langle B_{\parallel} \rangle$  map is not affected by the LOS depth, so that it exhibits the field strength and direction only, so that the RM singularity along the galactic plane does not



appear. The map reveals a widely extended arched region with positive magnetic strength of  $\langle B_{\parallel} \rangle \sim +5\mu\text{G}$  in the north from  $(l, b) \sim (40^\circ, 5^\circ)$  to  $(210^\circ, 0^\circ)$ . This arch seems to be continued by a negative strength arch with  $\langle B_{\parallel} \rangle \sim -5\mu\text{G}$  in the south from  $(l, b) \sim (50^\circ, -5^\circ)$  to  $(160^\circ, -30^\circ)$ .

It may be possible to connect the positive and negative  $B_{\parallel}$  arches to draw a giant loop, or a shell, from  $l \sim 40^\circ$  to  $220^\circ$  with the field direction being reversed from north to south. Alternatively, the positive arch may be traced through the empty sky around the south pole in the present data (Taylor et al. 2009), where the improved map shows positive RM (Oppermann et al. 2012). If this is the case, the RM arches may trace a sinusoidal belt from the southern hemisphere in the 1st and 2nd quadrants to northern in the 3rd and 4th quadrants, drawing an  $\infty$  shaped belt on the sky, with the necks in the galactic plane at  $l \sim 30^\circ$  and  $240^\circ$ . The arched magnetic region along the Aquila Rift from  $(l, b) \sim (30^\circ, -10^\circ)$  to  $(300^\circ, +30^\circ)$  with  $\langle B_{\parallel} \rangle \sim +2$  to  $-4\mu\text{G}$  could be a part of the  $\infty$  belt.

It is also interesting to note that both the northern and southern polar regions show positive  $B_{\parallel}$  with  $\langle B_{\parallel} \rangle \sim +1\mu\text{G}$ , indicating that the vertical (zenith) field directions are pointing away from the Sun.

## 4.2 Total intensity

The total magnetic intensity  $B_{\text{tot}}$  is calculated by assuming that the magnetic and cosmic ray energy densities are in equipartition as (see Appendix)

$$B^2/8\pi \sim N_{\text{CR}} E_{\text{cr}}, \quad (19)$$

where  $N_{\text{CR}}$  is the cosmic-ray electron number density and  $E_{\text{cr}}$  is representative energy of radio emitting cosmic rays. The magnetic strength is then related to the frequency  $\nu$  and volume emissivity  $\epsilon$  as

$$\left(\frac{\langle B_{\text{tot}} \rangle}{\mu\text{G}}\right) \sim 3.03 \times 10^8 Q \left(\frac{\nu}{\text{GHz}}\right)^{-1/7} \epsilon^{2/7}, \quad (20)$$

where,  $Q$  is an equipartition factor, which depends on various assumed conditions and source models. There have been decades of discussion about  $Q$  since Burbidge (1956), which includes dependence on such parameters as the spectral index, cut-off frequencies, proton-to-electron density ratio, volume filling factor, field orientation, and/or degree of alignment (e.g., Beck and Krause 2005). The emissivity  $\epsilon$  is related to  $L$  and  $T_{\text{syn}}$  through equation (5),

$$\left(\frac{\epsilon}{\text{erg cm}^{-3}\text{s}^{-1}}\right) \sim 6.796 \times 10^{-12} \left(\frac{T_{\text{syn}}}{\text{K}}\right) \left(\frac{\nu}{\text{GHz}}\right)^3 \left(\frac{L}{\text{pc}}\right)^{-1}. \quad (21)$$

The emissivity depends on the filling factor through  $\epsilon \propto L^{-1} \propto \eta^{-1/3}$ . So, we here introduce an  $\eta$ -corrected magnetic strength,

$$\mathcal{B}_{\text{tot}} \sim \eta^{2/21} \langle B_{\text{tot}} \rangle / Q. \quad (22)$$

For  $\eta \sim 0.035$  as measured in the previous section, we obtain  $\mathcal{B}_{\text{tot}} \sim 0.73 \langle B_{\text{tot}} \rangle / Q$ .

Figure 12 shows an all-sky map of the calculated total magnetic intensity  $\langle B_{\text{tot}} \rangle / Q$ . Except for discrete radio sources including radio spurs and GC, the map shows a smooth local magnetic intensity within  $\sim 200$  pc. Local magnetic strengths were calculated in intermediate latitude regions at  $+30^\circ \leq b \leq +70^\circ$  and  $-70^\circ \leq b \leq -30^\circ$  to obtain  $B_{\text{tot}}/Q = 10.7 \pm 3.1\mu\text{G}$  and  $10.3 \pm 2.7\mu\text{G}$ , respectively. Combining the two regions, we obtain  $B_{\text{tot}}/Q = 10.5 \pm 3.0\mu\text{G}$ . By correcting for the volume filling factor

( $\eta^{2/21} = 0.73$ ), we obtain a representative local field strength of  $\mathcal{B}_{\text{tot}} = 7.6 \pm 2.1\mu\text{G}$  for  $Q = 1$ .

Given  $\langle B_{\text{tot}} \rangle$  and  $\langle B_{\parallel} \rangle$  maps, the perpendicular component of the magnetic field is easily calculated by  $\langle B_{\perp} \rangle \sim \sqrt{\langle B_{\text{tot}} \rangle^2 - \langle B_{\parallel} \rangle^2}$ . However, the accuracy of the above estimated  $\langle B_{\text{tot}} \rangle$  would be too poor to obtain a meaningful map of the perpendicular component.

## 5 DISCUSSION

### 5.1 Summary

The latitudinal plots in figure 2 indicate that the four observables,  $RM$ ,  $T_{\text{syn}}$ ,  $T_{\text{ff}}$ , and  $N_{\text{HI}}$ , are tightly correlated with each other through their cosec  $|b|$  variations. This indicates that the distributions of the sources and their physical parameters are also tightly correlated with each other. Based on this fact, the sources of these emissions and Faraday rotation are assumed to be distributed in a single local disk in the Galaxy.

On this assumption, some useful relations were derived for calculating the local ISM quantities such as magnetic strength  $\langle B_{\text{tot}} \rangle$ , and LOS component of magnetic field  $\langle B_{\parallel} \rangle$ , thermal electron density  $\langle n_e \rangle$ , HI density  $\langle n_{\text{HI}} \rangle$ , and LOS depth  $L$ , or the scale thickness  $z_{1/2}$  and  $z_{1/2:\text{disk}}$  with the volume filling factor  $\eta$ . It was emphasized that determination of  $L$  plays an essential role in the present hybrid method to calculate the physical quantities, while only  $\langle B_{\parallel} \rangle$  can be directly calculated from  $RM$  and  $N_{\text{HI}}$  without being affected by  $L$ .

Applying the method to archival radio data, all-sky maps of  $\langle B_{\parallel} \rangle$  and  $\langle B_{\text{tot}} \rangle$  were obtained, which revealed a detailed magnetic structure in the local interstellar space within the Galactic disk near the Sun. The  $\langle B_{\parallel} \rangle$  map showed that the magnetic direction varies sinusoidally along a giant arch-shaped belt on the sky, changing its LOS direction from north to south and vice versa every two galactic quadrants. Maximum parallel component of  $\sim \pm 5 - 6\mu\text{G}$  was observed on the belt at intermediate latitudes. The  $\langle B_{\text{tot}} \rangle$  map showed that the total magnetic strength is smoothly distributed on the sky, and the averaged value was obtained to be  $\langle B_{\text{tot}} \rangle / Q \sim 10.5\mu\text{G}$  in the intermediate latitude region. Assuming an equipartition factor of  $Q = 1$ , we obtained an  $\eta$ -corrected field strength of  $\mathcal{B}_{\text{tot}} \sim 7.6\mu\text{G}$  for the measured volume-filling factor of  $\eta \sim 0.035$ .

### 5.2 Dependence on the thermal electron fraction

The proportionality of the densities of thermal electrons and HI gas is confirmed through the tight correlation between  $N_{\text{HI}}$  and  $T_{\text{ff}}$  ( $EM$ ) by figures 2 and 3. On this basis, we assumed a constant thermal electron fraction of  $x_e \sim 0.1$  close to the current measurement on the order of  $\sim 0.08$  (Foster et al. 2013). However,  $x_e$  affects the result through equation (17), where  $L \propto x_e^2$  and it propagates to the other quantities as  $\langle B_{\parallel} \rangle \propto x_e^{-1}$ ,  $\langle B_{\text{tot}} \rangle \propto x_e^{-4/7}$ ,  $\langle n_e \rangle \propto x_e^{-1}$ , and  $\langle n_{\text{HI}} \rangle \propto x_e^{-2}$ . Namely, the ISM quantities are generally proportional inversely to  $x_e$ , with strongest effect on  $\langle n_{\text{HI}} \rangle$  and weakest on  $\langle B_{\text{tot}} \rangle$ .

### 5.3 Uncertainty from energy equipartition

The most uncertain point in the present analysis is the estimation of magnetic strength from the energy equipartition of cosmic-ray electrons and magnetic field. Since the equipartition factor  $Q$  is still

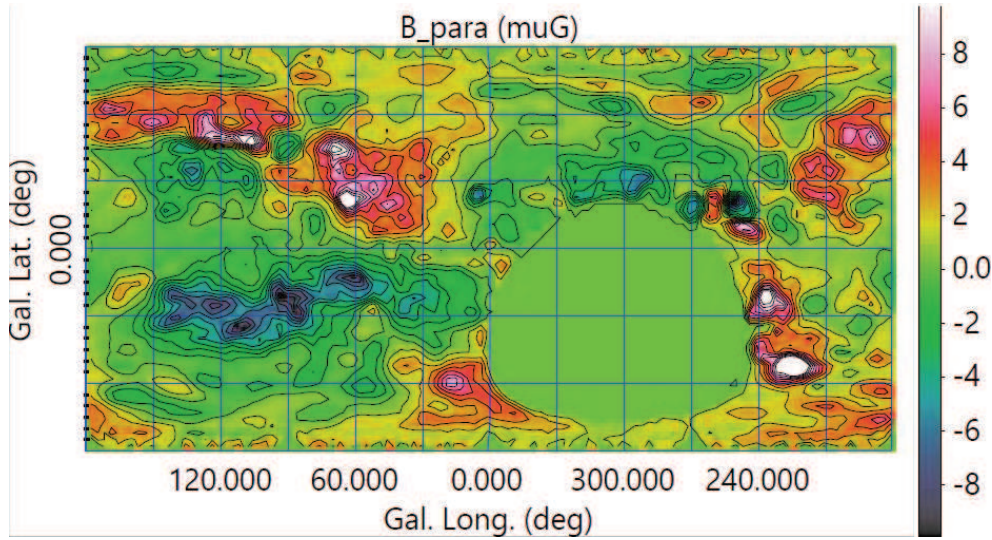


**Figure 11.** All-sky maps of  $\langle B_{\parallel} \rangle$  with contours at interval of  $1 \mu\text{G}$ . Positive value with red color indicates a field away from the observer, and negative with blue, approaching.

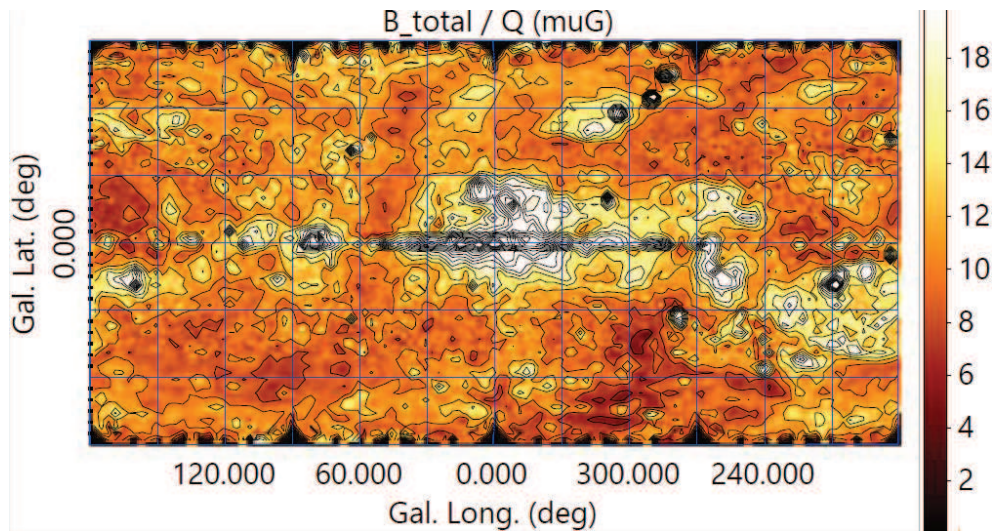


**Figure 12.** All-sky maps of  $\langle B_{\text{tot}} \rangle / Q$  with contours at interval of  $2 \mu\text{G}$ . The  $\eta$ -corrected strength is obtained by  $\mathcal{B}_{\text{tot}} \sim 0.72 \times$  map values.

open to discussion, the obtained total magnetic intensities should be taken only as a reference to see the relative distribution of the strength on the sky.

Also, the single disk assumption for synchrotron and thermal components may break at high latitudes. As in figure 3, the plots of  $T_{\text{syn}}$  against  $N_{\text{HI}}$  and  $T_{\text{ff}}$  bend at high latitudes, showing an order of magnitude excess at high latitudes over smooth extension from the disk component. The synchrotron excess over that expected from frozen-in assumption is about  $\delta T_{\text{syn}} \sim 0.1 \text{ K}$ .

In figure 13 we plot  $T_{\text{syn}} - \delta T_{\text{syn}}$  mimicking *halo-subtracted* synchrotron emission, which is well fitted by a power law expected from low and intermediate latitude regions. This fact suggests that the energy-equipartition holds inside the disk, whereas a non-thermal halo at  $\sim 0.1 \text{ mK}$  level at  $23 \text{ GHz}$  is extending outside the gas disk.

#### 5.4 Effect of inhomogeneity

From the tight cosec  $|b|$  relation of the used radio observables, for which no extinction problem exists, we assumed a uniform layered disk of ISM. In more realistic conditions, however, the layer may be more or less not uniform, and the assumption made in equations (6-8) may not hold, or must be modified.

However, it is emphasized that 'clumpy' inhomogeneity does not affect the 'effective' LOS depth  $L$  by definition, because  $L$  already includes the volume filling factor. Hence, the determined values of the ISM, which are averages of values 'inside' the clumps (or within  $L$ ), are not affected by the inhomogeneity.

The assumption made for equations 6 to 8 will not hold exactly in a disk with globally varying density with the height. For example, if the functions  $f$  and  $g$  are represented by a Gaussian function of the height from the galactic plane, we have  $\langle f \rangle \sim 1.1 \langle f^2 \rangle^{1/2}$  and  $\langle fg \rangle \sim 1.2 \langle f \rangle \langle g \rangle$ . For a cosh<sup>-2</sup> function, as for self-gravitating



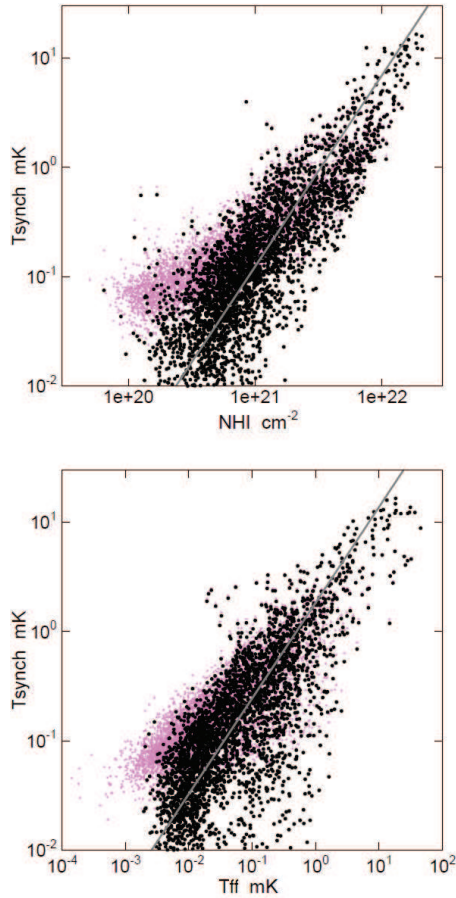


**Figure 13.** Correlation of  $T_{\text{syn}} - 0.1$  mK with  $N_{\text{HI}}$  and  $T_{\text{ff}}$ , which are approximately represented by a power law of index  $7/4$  and  $7/8$ , respectively. Vertical scaling of the lines are arbitrary. Original data are shown in violet.

disk, the factors are 1.2 and 1.4, respectively. These factors propagate onto the results, yielding uncertainty by a factor of  $\sim 1.1 - 1.2$  for quantities having linear dependence on the distance, and by 1.2 – 1.4 to those with non-linear dependence such as  $RM$  and  $EM$ . However, the finally determined  $B$  and  $n_e$  or  $n_{\text{HI}}$  are more linearly dependent on the distance, and hence their uncertainties may be about a factor of  $\sim 1.1 - 1.2$  at most.

### 5.5 Local bubble

A large-scale irregularity of the ISM has been reported as a local bubble (Bochkarev 1992; Lallement et al. 2003; Liu et al. 2017; Alves et al. 2018), which makes a cavity around the Sun of radius  $r_{\text{bub}} \sim 100 - 200$  pc widely open to the galactic halo. Then, a difficulty is encountered to explain the tight cosec  $|b|$  relation in figure 2. In order for the cosec relation to hold up to  $b \sim \pm 80^\circ$  at least, the scale height of the galactic disk must be greater than  $\sim r_{\text{bub}} \tan 80^\circ \sim 600$  pc to 1.2 kpc, which is obviously not the case. If the disk scale height is  $\sim 200$  pc as measured in HI, the open cavity should result in huge empty sky in radio around the galactic poles, which also appears not the case.

In figure 14 we compare the cosec  $|b|$  relation observed for  $N_{\text{HI}}$  with cavity models mimicking the local bubble. Line A indicates a Gaussian disk of scale height 200 pc without bubble; B represents a case with a spherical bubble of radius 100 pc in the

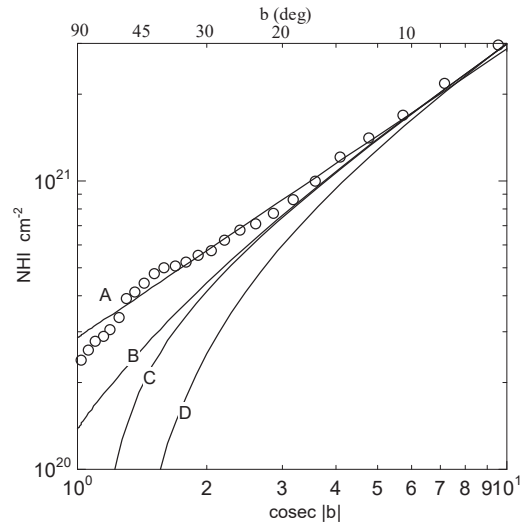


**Figure 14.** Cosec  $|b|$  relation of the HI disk from figure 2 (averaged values every  $2^\circ$  by circles) compared with (A) a model of Gaussian disk of scale height 200 pc without bubble; (B) same disk with a spherical bubble of radius 100 pc; (C) and (D) disk with vertical cylindrical cavity of radius 100 and 200 pc, respectively. Values are normalized to the observation at  $b \sim 5^\circ$ .

Gaussian disk of scale height 200 pc, and C and D for cylindrical cavity of radius 100 and 200 pc, respectively. Model C may be compared with the result by Lallement et al. (2003), which appears significantly displaced from the cosec  $|b|$  relation. Such is found not only in HI, but also in thermal and synchrotron emissions, and Faraday RM (figure 2). Therefore, the relation between the local bubble and the cosec  $|b|$  disk in radio remains as a question.

### 5.6 Other observables

Molecular gas has not been taken into account in this study, because the nearest molecular clouds within LOS depths concerned in this paper are rather few (Knude and Hog 1998). Comparison with a local bubble surrounded by dusty clouds (e.g., Lallement et al. 2003), besides the cosec  $|b|$  problem, would be an interesting subject, although the present analysis gives only averaged values along the LOS within  $L$ , and hence cannot be directly compared with the 3D study.

Polarization data in radio and infrared observations were not used, although they are obviously useful to improve the present hybrid analysis. Inclusion of these observables is beyond the scope of this paper, for which more sophisticated analyses would be required.

### 5.7 Local magnetic topology

Despite of the various uncertainties as above, we emphasize that the projected topology of  $B_{\parallel}$  mapped in figure 11 is rather certain. Although the  $\infty$ -shaped variation of  $RM$  might sound a bit strange, we could speculate possible topology of the magnetic lines of force in the local space.

The field direction reverses about the galactic plane from north to south in a wide range from  $l \sim 30^\circ$  to  $\sim 210^\circ$ . The  $B_{\parallel}$  value attains its maximum and minimum at both intermediate latitudes around  $(l, b) \sim (130^\circ, \pm 30^\circ \sim 50^\circ)$ . Such  $RM$  behavior on the sky

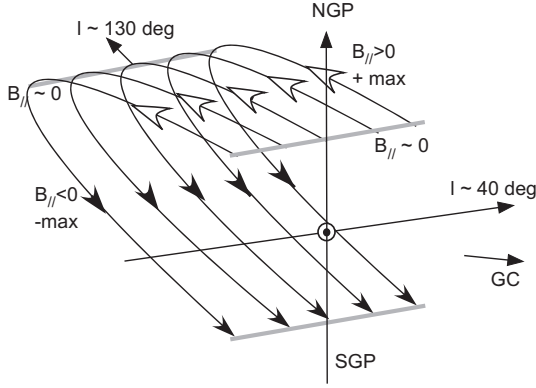


**Figure 15.** Possible topology of local magnetic lines of force to explain  $B_{||}$  map in figure 11.

could be explained by a reversed topology of local field as illustrated in figure 15.

## ACKNOWLEDGMENTS

We thank the authors of the LAB HI survey (Dr. Kalberla et al. ), all-sky rotation measure map (Dr. Taylor et al. ), and the WMAP 7 years maps (Dr. Gold et al. ) for the archival data. The data analyses were performed on a computer system at the Astronomical Data Center of the National Astronomical Observatories of Japan.

## REFERENCES

- Akahori T., et al., 2018, PASJ, 70, R2  
 Alves M. I. R., Boulanger F., Ferrière K., Montier L., 2018, A&A, 611, L5  
 Bochkarev N. G., 1992, A&AT, 3, 3  
 Beck R., Krause M., 2005, AN, 326, 414  
 Burbidge G. R., 1956, ApJ, 124, 416  
 Foster T., Kothes R., Brown J. C., 2013, ApJ, 773, L11  
 Fukui Y., Hayakawa T., Inoue T., Torii K., Okamoto R., Tachihara K., Onishi T., Hayashi K., 2018, ApJ, 860, 33  
 Gold B., et al., 2011, ApJS, 192, 15  
 Kalberla P. M. W., Burton W. B., Hartmann D., Arnal E. M., Bajaja E., Morras R., Pöppel W. G. L., 2005, A&A, 440, 775  
 Kalberla P. M. W., Dedes L., Kerp J., Haud U., 2007, A&A, 469, 511  
 Knude J., Hog E., 1998, A&A, 338, 897  
 Lallement R., Welsh B. Y., Vergely J. L., Crifo F., Sfeir D., 2003, A&A, 411, 447  
 Landau, L. D. and Lifshitz, E. M. 1971, in *The Classical Theory of Fields*, 3rd ed., Chap. 9, Pergamon Press, Oxford.  
 Levine E. S., Blitz L., Heiles C., 2006, ApJ, 643, 881  
 Liu W., et al., 2017, ApJ, 834, 33  
 Lockman F. J., 1984, ApJ, 283, 90  
 Mao S. A., et al., 2012, ApJ, 755, 21  
 Marasco A., Fraternali F., van der Hulst J. M., Oosterloo T., 2017, A&A, 607, A106  
 Moffet, A. T. 1975, in *Galaxies and the Universe*, ed. Sandage, A., Sandage, M., and Kristian, J., Stars and Stellar Systems Vol. 9, Chap. 7, Chicago Univ. Press., Chicago. <https://archive.org/details/GalaxiesAndTheUniverse/page/n259>

- Nakanishi H., Sofue Y., 2016, PASJ, 68, 5  
 Oppermann N., et al., 2012, A&A, 542, A93  
 Oster L., 1961, AJ, 66, 50  
 Sofue Y., 2017, MNRAS, 468, 4030  
 Sofue Y., 2018, PASJ, 70, 50  
 Sofue Y., Fujimoto M., Wielebinski R., 1986, ARA&A, 24, 459  
 Sofue Y., Nakanishi H., 2017, MNRAS, 464, 783  
 Stil J. M., Taylor A. R., Sunstrum C., 2011, ApJ, 726, 4  
 Sun X. H., et al., 2015, ApJ, 811, 40  
 Taylor A. R., Stil J. M., Sunstrum C., 2009, ApJ, 702, 1230  
 Van Eck C. L., et al., 2017, A&A, 597, A98  
 Wolleben M., et al., 2010, ApJ, 724, L48  
 Wouterloot J. G. A., Brand J., Burton W. B., Kwee K. K., 1990, A&A, 230, 21

## APPENDIX A: EQUIPARTITION

### A1 $B$ , $E$ , and $N(E)$ by $\varepsilon$ and $\nu$

The equipartition between magnetic and cosmic-ray pressure relates the magnetic strength  $B$ , representative energy  $E$  and density  $N(E)$  of cosmic-ray electrons responsible for synchrotron emission at observing frequency  $\nu$  and volume emissivity  $\varepsilon$  (Burbidge 1956; Moffet 1975; Sofue et al. 1986 for review). We here write down the basic relations among  $B$ ,  $N(E)$  and  $E$ , which are used to calculate the 'reference value' of  $B$  for  $Q = 1$  in equation 20.

$$\frac{B^2}{8\pi} \sim EN(E), \quad (\text{A1})$$

$$\nu \sim \frac{e}{4\pi m_e^3 c^5} BE^2, \quad (\text{A2})$$

and

$$\varepsilon \sim -\frac{dE}{dt} N(E) \sim \frac{2e^4}{3m_e^4 c^7} B^2 E^2 N(E) \quad (\text{A3})$$

(e.g., Landau and Lifshitz 1971). These equations can be solved for  $B$  in terms of  $\nu$  and  $\varepsilon$  as

$$\left(\frac{B}{\mu\text{G}}\right) \sim 3.03 \times 10^8 \left(\frac{\nu}{\text{GHz}}\right)^{-1/7} \left(\frac{\varepsilon}{\text{erg cm}^{-3}\text{s}^{-1}}\right)^{2/7}. \quad (\text{A4})$$

Moffet (1973) gave a coefficient  $3.25 \times 10^8$  for a radio spectral index of  $\alpha = -0.75$ .

As a byproduct, we obtain

$$\left(\frac{N(E)}{\text{cm}^{-3}}\right) \sim 2.91 \times 10^9 \left(\frac{\nu}{\text{GHz}}\right)^{-6/7} \left(\frac{\varepsilon}{\text{erg cm}^{-3}\text{s}^{-1}}\right)^{5/7}, \quad (\text{A5})$$

and

$$\left(\frac{E}{\text{erg}}\right) \sim 1.26 \times 10^{-6} \left(\frac{\nu}{\text{GHz}}\right)^{4/7} \left(\frac{\varepsilon}{\text{erg cm}^{-3}\text{s}^{-1}}\right)^{-1/7}. \quad (\text{A6})$$

### A2 $T_{\text{syn}}$ by $N_{\text{HI}}$

Using equations (4), (A1) and (A2),  $T_{\text{syn}}$  is expressed in terms of  $L$  and  $B$  as

$$T_{\text{syn}} \propto LB^{9/2}. \quad (\text{A7})$$

Assuming that the HI gas has a constant velocity dispersion ( $\sigma \sim$  constant) and is in pressure (energy density) balance with magnetic field as

$$\frac{B^2}{8\pi} \sim \frac{1}{2} m_{\text{H}} n_{\text{HI}} \sigma^2 \propto n_{\text{HI}}, \quad (\text{A8})$$

we have

$$B \propto n_{\text{HI}}^{1/2} \sim (N_{\text{HI}}/L)^{1/2}. \quad (\text{A9})$$

Inserting this to equation (A7),

$$T_{\text{syn}} \propto n_{\text{HI}}^{1/4} N_{\text{HI}}^{7/4}. \quad (\text{A10})$$

While column density  $N_{\text{HI}}$  is highly variable with  $b$  and  $L$ , the volume density  $n_{\text{HI}}$  is not, and appears by a weak power of index 1/4. So, we may approximate  $T_{\text{syn}}$  by

$$T_{\text{syn}} \propto N_{\text{HI}}^{7/4}. \quad (\text{A11})$$